Available online at www.sciencedirect.com
ScienceDirect
Trans. Nonferrous Met. Soc. China 35(2025) 3480−3492
Transactions of Nonferrous Metals Society of China
www.tnmsc.cn

Enhancing iron and titanium recovery efficiency via coal-based direct reduction of vanadium−titanium magnetite raw ore

Zheng-hao WANG, Si-yu CHEN, Liang CHEN, Bin LIANG, Dong-mei LUO

School of Chemical Engineering, Sichuan University, Chengdu 610065, China

Received 4 January 2024; accepted 6 August 2024

Abstract: An approach for coal-based direct reduction of vanadium−titanium magnetite (VTM) raw ore was proposed. Under the optimal reduction conditions with reduction temperature of 1140 °C, reduction time of 3 h, C-to-Fe molar ratio of 1.2:1, and pre-oxidation temperature of 900 °C, the iron metallization degree is 97.8%. Ultimately, magnetic separation yields an iron concentrate with an Fe content of 76.78 wt.% and efficiency of 93.41%, while the magnetic separation slag has a Ti grade and recovery of 9.36 wt.% and 87.07%, respectively, with a titanium loss of 12.93%. This new strategy eliminates the beneficiation process of VTM raw ore, effectively reduces the Ti content in the iron concentrate, and improves the comprehensive utilization of valuable metals.

Key words: vanadium−titanium magnetite; raw ore; reduction; pre-oxidation; metallic iron

1 Introduction

Vanadium−titanium magnetite (VTM) is a complex mineral containing iron (Fe), titanium (Ti), and vanadium (V) as its principal constituents [1,2]. Additionally, these VTM deposits contain significant amounts of other valuable elements, including but not limited to scandium (Sc), cobalt (Co), and nickel (Ni) [3]. Consequently, the exploration and investigation of processes aimed at the efficient and comprehensive utilization of V and Ti magnetite resources assume paramount significance.

Currently, the blast furnace (BF) method is the predominant approach used for the treatment of VTM in China [4,5]. The BF ironmaking process is typically coupled with the converter V extraction process to leverage both methodologies. In this technique, the VTM concentrate, following sintering and pelletizing, is introduced into the BF for high-temperature smelting, ultimately producing vanadium-bearing hot metal and titanium-rich BF slag through the selective reduction and separation process [6−8]. The subsequent step involves subjecting the vanadium-bearing hot metal to converter blowing, resulting in the formation of semi-steel and vanadium slag [9−12]. The hydro-metallurgical methods can then be employed to extract the vanadium slag, whereas the semi-steel can undergo further treatment to yield qualifying steel [13,14]. The BF method boasts notable advantages, including unparalleled scalability and superior production efficiency, facilitating recoveries of up to 90% and 70% for Fe and V, respectively [15,16]. However, despite these merits, a substantial quantity of BF slag, with a considerable 22% TiO_2 content, remains underutilized, leading to concerns about resource wastage and environmental pollution [17]. Moreover, the environmental consequences arising from the substantial energy consumption and carbon

Corresponding author: Dong-mei LUO, Tel: +86-13981926059, E-mail: dmluo@scu.edu.cn
https://doi.org/10.1016/S1003-6326(25)66894-4

dioxide (CO_2) emissions associated with the BF method are increasingly worrisome [18]. Consequently, the development of non-blast furnace processes emerges as an imperative course of action.

The coal-based direct reduction−magnetic separation stands as a prevalent non-blast furnace method [19−21]. This method involves selectively reducing iron oxides present in VTM concentrates to metallic iron while retaining V and Ti in oxide form [22]. By regulating the reduction conditions, the growth of iron particles is facilitated, enabling subsequent separation of magnetic metallic iron from the non-magnetic slag containing V and Ti through grinding and magnetic separation techniques. Recent research in the VTM reduction primarily centers on VTM concentrate as the key raw material [23−27]. However, this method falls short, with only about 13% of Ti being incorporated into the ilmenite concentrate post sorting procedures for obtaining the VTM concentrate [28]. Notably, over 30% of Ti and other valuable elements end up in the tailings, posing challenges for their utilization [29,30]. To overcome these limitations, the direct use of VTM raw ore as the primary material for reduction and extraction was proposed in this study. This approach not only obviates the need for beneficiation processes but also ensures that both V and Ti can enter the extraction phase, substantially enhancing raw material utilization efficiency.

This study introduces an innovative utilization of VTM raw ore in coal-based direct reduction for the first time. The reduction conditions were systematically investigated and the effect of the substantial silicate impurities present in the raw ore on the formation and growth of metallic iron was analyzed. Recognizing the challenge posed by the small size of iron particles during the reduction process of raw ore, a pre-oxidation step was introduced to enhance the reduction process. In addition, the fundamental principles governing the formation and growth of iron particles in the reduction process of raw ore were elucidated.

2 Experimental

2.1 Materials

The experimental materials employed in this study, including the VTM raw ore, iron concentrate, and ilmenite concentrate, were generously provided by the Panzhihua Iron & Steel Company in China. Table 1 presents the chemical compositions of the raw materials. Notably, the VTM raw ore exhibits lower grades of TFe, TiO_2, and V_2O_5 at 23.73%, 11.33%, and 0.19%, respectively, in contrast to the iron concentrate, which registers at 51.68%, 12.77%, and 0.52%. Additionally, the TFe and TiO_2 contents in the VTM raw ore are lower than those in the ilmenite concentrate (27.49% and 44.55%). Additionally, the raw ore contains a significant amount of impurities such as Ca, Mg, Si, and Al, thereby contributing to its intricate and diverse composition. The XRD patterns (Fig. 1) depicted that the mineralogical compositions in the raw ore are magnetite (Fe_3O_4), ilmenite ($FeTiO_3$), feldspar ($(Ca,Na)(Si,Al)_2Si_2O_8$), augite $Ca(Ti,Mg,Fe,Al)$-$(Si,Al)_2O_6$) and chlorite ($(Mg,Al)_6(Si,Al)_4O_{10}(OH)_{10}$). Comparatively, the iron and titanium concentrates exhibit fewer impurities and are primarily composed of Fe_3O_4 and $FeTiO_3$, respectively. Bituminous coal served as the reducing agent, and all other chemicals used were of analytical grade.

The ash melting point of the raw ore mixed with bituminous coal was determined using a microcomputer-controlled intelligent ash fusion point tester (model TJHR−6000) to establish the maximum reaction temperature, and the results are depicted in Fig. 2. After the addition of bituminous coal, the ash melting temperature of the raw ore increased. To maintain the reduction reaction of the VTM raw ore as a solid-phase reaction, the reduction temperature should not exceed 1140 °C.

Table 1 Chemical composition of raw ore, iron concentrate, and ilmenite concentrate (wt.%)

Sample	TFe	V_2O_5	TiO_2	SiO_2	Al_2O_3	CaO	MgO	Others
Raw ore	23.73	0.19	11.33	25.84	11.03	6.70	10.75	0.16
Pre-oxidized raw ore	23.05	0.21	11.67	26.46	11.15	6.77	10.54	0.18
Iron concentrate	51.68	0.52	12.77	3.97	4.29	0.88	3.23	0.09
Ilmenite concentrate	27.49	0.10	44.55	6.09	2.42	1.09	5.63	0.34

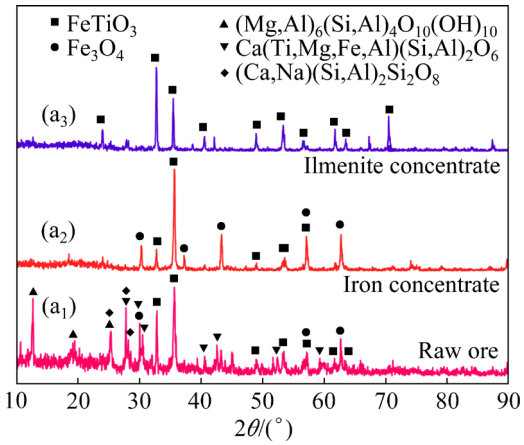

Fig. 1 XRD patterns of mineral materials: (a_1) Raw ore; (a_2) Iron concentrate; (a_3) Ilmenite concentrate

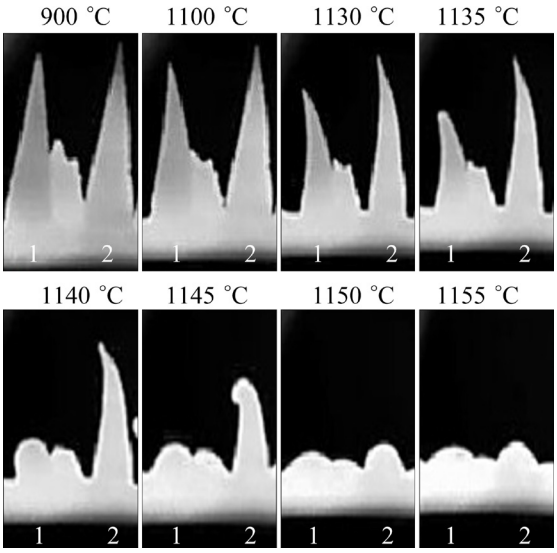

Fig. 2 Ash melting point of (1) raw ore and (2) raw ore mixed with bituminous coal

2.2 Experimental procedures

2.2.1 Coal-based direct reduction

Analyzing the reduction process of VTM raw ore directly poses challenges due to its intricate composition. Nevertheless, it can be regarded as a composite mineral consisting of titanium concentrate, iron concentrate, and veinstone tailings. Investigating the reduction processes of titanium concentrate and iron concentrate, which exhibit relatively simpler physical structures, can yield valuable insights into the behavior of VTM raw ore. In each experiment, 30 g mineral powder was meticulously mixed with the corresponding coal powder in a graphite crucible. Subsequently, the crucible was introduced into the tubular furnace, with temperature elevating at a rate of 10 °C/min (5 °C/min for temperatures exceeding 800 °C), and maintained in the target temperature range of 950−1140 °C for a predefined duration. Nitrogen (N_2) was employed as a protective gas throughout the reaction. Upon completion of the reaction, the sample was cooled to room temperature in an inert atmosphere before being extracted for subsequent analysis. The metallic iron content in the reduction products was determined using the potassium dichromate titration method as described in Part A in Supporting Information (SI). The metallization degree was calculated as Eq. (1):

$$\eta=\frac{\mathrm{MFe}}{\mathrm{TFe}}\times 100\% \tag{1}$$

where η is the metallization degree (%), MFe is the mass fraction of the metallic iron in the reduced sample, and TFe the mass fraction of the total iron in reduced sample.

2.2.2 Enhanced reduction by pre-oxidation

Before the reduction experiments, a pre-oxidation procedure was carried out on the raw ore. The raw material was placed in a muffle furnace in an air atmosphere with a controlled temperature increase rate of 10 °C/min, followed by a specified holding period. Subsequently, it was blended with coal powder for the reduction experiments.

2.2.3 Magnetic separation

The magnetic separation experiment was performed on a magnetic separator to isolate magnetic and non-magnetic components. After crushing and grinding, 8 g of the reduced samples were subjected to wet ball milling with a ball-to-material ratio of 12:1 and a slurry ratio of 4:1. The resultant slurry from wet ball milling was promptly subjected to magnetic separation using a magnetic separator (XCGS−50, Yongsheng Environmental Protection Machinery Factory, Jiangxi Province, China), operating under the specified magnetic separation conditions. The recovery of Fe and Ti in the magnetic separation process was calculated as follows:

$$R_1=\frac{w_1\cdot m_1}{w\cdot m}\times 100\% \tag{2}$$

where R_1 is the recovery of Fe and Ti (%), w_1 is content of Fe and Ti in magnetic separation slag (%), m_1 is the mass of magnetic separation slag (g), w is the amount of Fe and Ti in the reduced sample (%), and m is the mass of the reduced sample (g).

2.3 Chemical analysis

The raw ore and reduced sample were melted with sodium dioxide (Na_2O_2) and NaOH at 750 °C for 30 min, and then leached with diluted hydrochloric acid, whereafter the Fe, Ti, V content in solution was detected by ICP-OES (ICP-OES, 7400, Thermo-Scientific, USA). The compositions of other elements in ore were measured by an X-ray fluorescence spectrometer with a Rh K_α radiation source (XRF−180, Shimadzu, Japan). The metal iron content in the reduced sample was determined by titration method. XRD analyses were performed using X-ray diffractometer (DX−2007, Danton, China) to collect data of the samples operating with Cu K_α in the 2θ range from 10° to 90°. The scanning electron microscope (SEM, ZeissSigma−300, Germany) was used to analyze the surface morphology of the solid samples. Melting point was measured by a microcomputer intelligent ash melting point tester (model TJHR−6000).

3 Results and discussion

3.1 Thermodynamic analysis of coal-based direct reduction of raw ore

The direct reduction process of the raw ore encompasses two essential stages: the solid-phase reduction of coal and the indirect reduction reaction involving carbon gasification. This reduction process generates both CO and CO_2. Notably, CO_2 can undergo a reaction with coal, resulting in the production of CO. This generated CO serves as a reducing gas, actively participating in the chemical reactions between iron oxides and titanium-iron oxides, thus enabling the indirect reduction process between gaseous and solid phases. To evaluate the thermodynamics of potential reactions within a coal-based reduction system, thermodynamic calculations were conducted using the software HSC 9.0, and the results are summarized in Table 2 and Fig. 3.

The Gibbs free energy gradients of the carbon thermal reduction reactions in the solid phase exhibit a negative correlation with increasing temperature (Fig. 3(a)), indicating that elevated temperatures promote more favorable reduction reactions. Notably, the Gibbs free energy values for these reactions become negative when the temperature exceeds 750 °C. Furthermore, in accordance with Reaction (14), the titanium−iron spinel ($FeTi_2O_5$) undergoes a transformation during the reduction process, resulting in the formation of Ti_3O_5 solid solution. This transformation promotes the solidification of FeO and MgO present in the minerals, culminating in the formation of black titanium spinel, $(Mg,Fe)Ti_2O_5$. Consequently, achieving complete reduction of titanium−iron oxides from the original ore proves to be a formidable challenge. In the context of gas−solid phase reduction, all reduction reactions in the gas phase demonstrate feasibility at a temperature of 750 °C, with the exception of Reaction (18). In Reaction (18), the Gibbs free energy exceeds 0 when the temperature surpasses 600 °C, rendering it thermodynamically challenging to proceed. However, practical observations indicate that the reaction can still proceed due to the swift consumption of CO_2 generated during the reaction via the Budor reaction, coupled with the continuous

Table 2 Reactions of iron and titanium−iron oxides in coal-based reduction system

Solid phase reduction reaction		Gas−solid phase reduction reaction	
$Fe_2O_3+C=2FeO+CO(g)$	(3)	$Fe_2O_3+CO(g)=2FeO+CO_2(g)$	(16)
$Fe_2O_3+1/2C=2FeO+1/2CO_2(g)$	(4)	$Fe_3O_4+CO(g)=3FeO+CO_2(g)$	(17)
$Fe_3O_4+C=3FeO+CO(g)$	(5)	$FeO+CO(g)=Fe+CO_2(g)$	(18)
$Fe_3O_4+1/2C=3FeO+1/2CO_2(g)$	(6)	$Fe_2TiO_5+CO(g)=2FeO+TiO_2+CO_2(g)$	(19)
$FeO+C=Fe+CO(g)$	(7)	$FeTiO_3+CO(g)=2Fe+TiO_2+CO_2(g)$	(20)
$FeO+1/2C=Fe+1/2CO_2(g)$	(8)	$FeTi_2O_5+CO(g)=Fe+2TiO_2+CO_2(g)$	(21)
$Fe_2TiO_5+C=2FeO+TiO_2+CO(g)$	(9)	$FeTi_2O_5+5/3CO(g)=Fe+2/3Ti_3O_5+5/3CO_2(g)$	(22)
$Fe_2TiO_5+1/2C=2FeO+TiO_2+1/2CO_2(g)$	(10)	$C+CO_2=2CO(g)$	(23)
$FeTiO_3+C=2Fe+TiO_2+CO(g)$	(11)		
$FeTiO_3+1/2C=2Fe+TiO_2+1/2CO_2(g)$	(12)		
$FeTi_2O_5+C=Fe+2TiO_2+CO(g)$	(13)		
$FeTi_2O_5+1/2C=Fe+2TiO_2+1/2CO(g)$	(14)		
$FeTi_2O_5+5/3C=Fe+2/3Ti_3O_5+5/3CO(g)$	(15)		

production of the reducing gas CO. Therefore, the reduction of iron oxides and titanium-iron oxides is thermodynamically feasible at elevated temperatures.

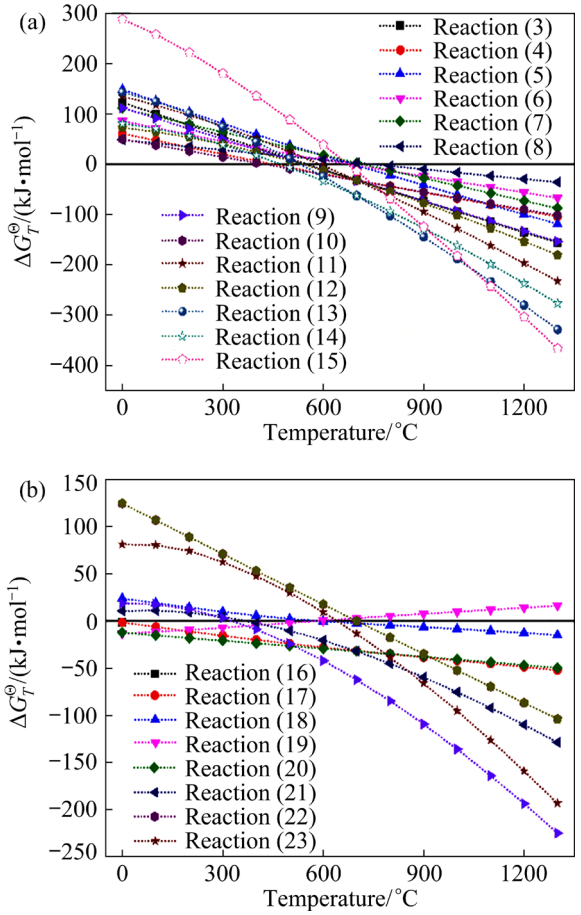

Fig. 3 $\Delta G_T^{\Theta} - T$ diagrams for main reactions of VTM raw ore: (a) In solid phase reduction process; (b) In gas−solid phase reduction process

3.2 Coal-based direct reduction of VTM raw ore

Figure 4(a) illustrates the effect of reduction temperature on the metallization degree of raw ore, titanium concentrate, and iron concentrate. The degree of metallization at each temperature follows the order: iron ore concentrate > raw ore > titanium concentrate. Notably, the metallization degree of iron concentrate reaches a maximum of 98.2% at 1000 °C, whereas that of raw ore and titanium concentrate reaches 91.8% and 81.1% at 1150 °C, respectively. The XRD pattern of the raw ore reduction products is heterogeneous, making it difficult to analyze a clear reduction process. Figure S1(a) in SI portrays the XRD patterns of the iron concentrate reduced samples at different temperatures. At 950 °C, the reduced sample exhibits metallic Fe peaks, along with some

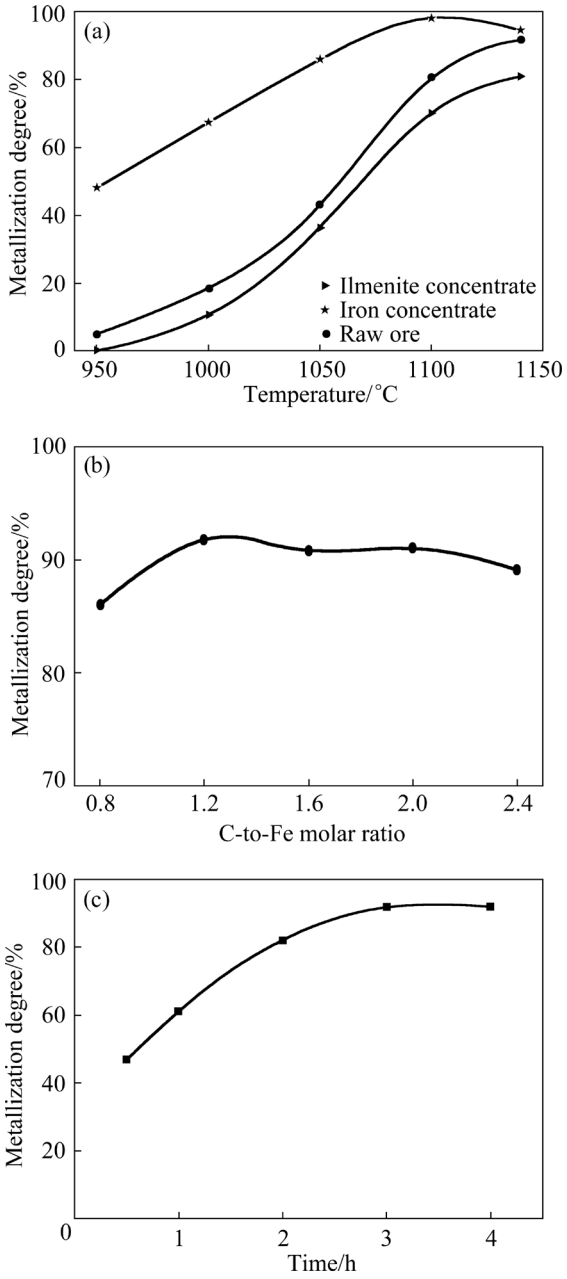

Fig. 4 (a) Effect of reduction temperature on metallization degree of raw ore, iron concentrate, and ilmenite concentrate; Effect of (b) C-to-Fe molar ratio and (c) reduction time on metallization degree of raw ore

unreacted Fe_3O_4. Upon elevating the temperature to 1000 °C, the new peak of $FeTiO_3$ is observed. Subsequently, as the temperature reaches 1100 °C, the $FeTiO_3$ peaks gradually diminish, and the presence of $(Mg,Fe)Ti_2O_5$ is detected. In light of thermodynamic analysis, it becomes evident that the structure of $(Mg,Fe)Ti_2O_5$ is relatively stable and less prone to complete reduction. This pivotal finding can elucidate the slightly lower metallization degree of the sample at 1140 °C.

Figure S1(b) in SI portrays the XRD patterns of titanium concentrate samples reduced at varying temperatures. A faint metallic Fe peak emerges at 1000 °C, signifying the initiation of reduction at this temperature. As the temperature increases, a large amount of $(Mg,Fe)Ti_2O_5$ phase is generated. It is plausible to posit that the presence of $(Mg,Fe)Ti_2O_5$ restricts further escalation of the metallization degree. In conclusion, the intermediate metallization degree observed in the raw ore can be attributed to the inclusion of ilmenite concentrate.

The effect of the C-to-Fe molar ratio on the metallization degree of the raw ore is depicted in Fig. 4(b). The highest metallization degree of 91.8% is achieved when the C-to-Fe molar ratio continues to increase to 1.2∶1. Figure 4(c) portrays the effect of the reduction time on the metallization degree of the raw ore. Prolonging the reduction time facilitates more complete reduction and the growth of metallic iron particles. The optimum reduction time is determined to be 3 h, which corresponds to a metallization degree of 91.8%. Furthermore, the XRD pattern of the reduced sample obtained under the optimized conditions is presented in Fig. 5. Notably, the disappearance of Fe_3O_4 and $FeTiO_3$ peaks in the reduction product suggests a substantial reduction of the raw ore. However, it is worth mentioning that the presence of the primary titanium-containing phase, denoted as $(Mg,Fe)Ti_2O_5$, is still observable. Conversely, the gangue phases of $(Ca,Na)(Si,Al)_2Si_2O_8$ and $Ca(Ti,Mg,Fe,Al)(Si,Al)_2O_6$ remain unchanged following the reduction, signifying their relative stability within the reaction system. On the contrary, the $(Mg,Al)_6(Si,Al)_4O_{10}(OH)_{10}$ component

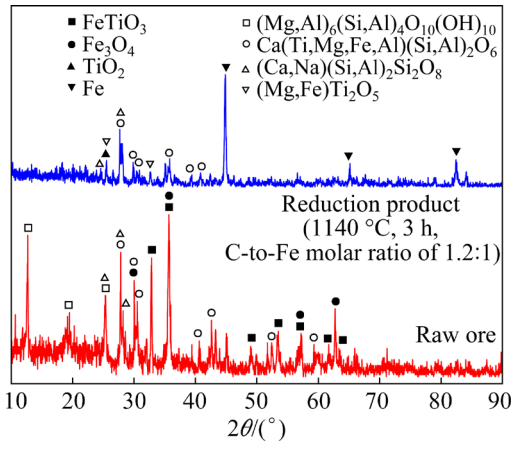

Fig. 5 XRD patterns of reduction product of raw ore

decomposes and disappears during the high-temperature reaction, leading to the generation of amorphous oxides.

Correspondingly, the microscopic morphology of the reduced samples derived from the iron concentrate, ilmenite concentrate, and raw ore is displayed in Fig. 6. Figure 6(a) exhibits the aggregation of metallic iron into larger particles within the reduced iron concentrate sample, with a distinct separation from titanium. In Fig. 6(b), the reduced ilmenite concentrate sample displays relatively smaller particle sizes for metallic Fe, likely attributed to the lower iron content and metallization degree. Additionally, due to the high titanium content in titanium concentrate and the formation of $(Mg,Fe)Ti_2O_5$ during the reduction process, some Fe particles are distributed with Ti. As a result, the reduction of ordinary iron oxides and titanium−iron oxides present in VTM raw ore follows two distinct pathways:

$$Fe_2O_3 \rightarrow Fe_3O_4 \rightarrow FeO \rightarrow Fe \quad (24)$$

$$Fe_2TiO_5 \rightarrow FeTiO_3 \rightarrow FeO/Ti_3O_5TiO_2 \rightarrow Fe \rightarrow (Mg,Fe)Ti_2O_5 \quad (25)$$

As shown in Fig. 6(c), it is evident that metallic iron obtained directly from the raw ore is primarily embedded as nearly spherical individual particles on the surface of other minerals. By analyzing the EDS analysis presented in Fig. S2 in SI, it is apparent that the dominant mineral composition comprises silicate gangue. Since the gangue materials do not actively participate in the reduction reaction, it can be inferred that the metallic iron formed during the reduction process comes into contact with a substantial amount of gangue within the original ore during the aggregation process, and these gangues can prevent it from forming larger metallic iron particles and ultimately embedded on its surface.

In conclusion, the optimum reduction conditions are reduction temperature of 1140 °C, reduction time of 3 h, and C-to-Fe molar ratio of 1.2∶1, corresponding to the maximum metallization degree of 91.8%. The partial reduction of iron oxide particles encapsulated within the gangue results in a diminished interfacial contact area with the reducing agent, thereby impeding the efficiency of the reduction process. Furthermore, the small size of the metallic iron particles poses challenges in achieving their complete separation from non-magnetic minerals in subsequent beneficiation steps.

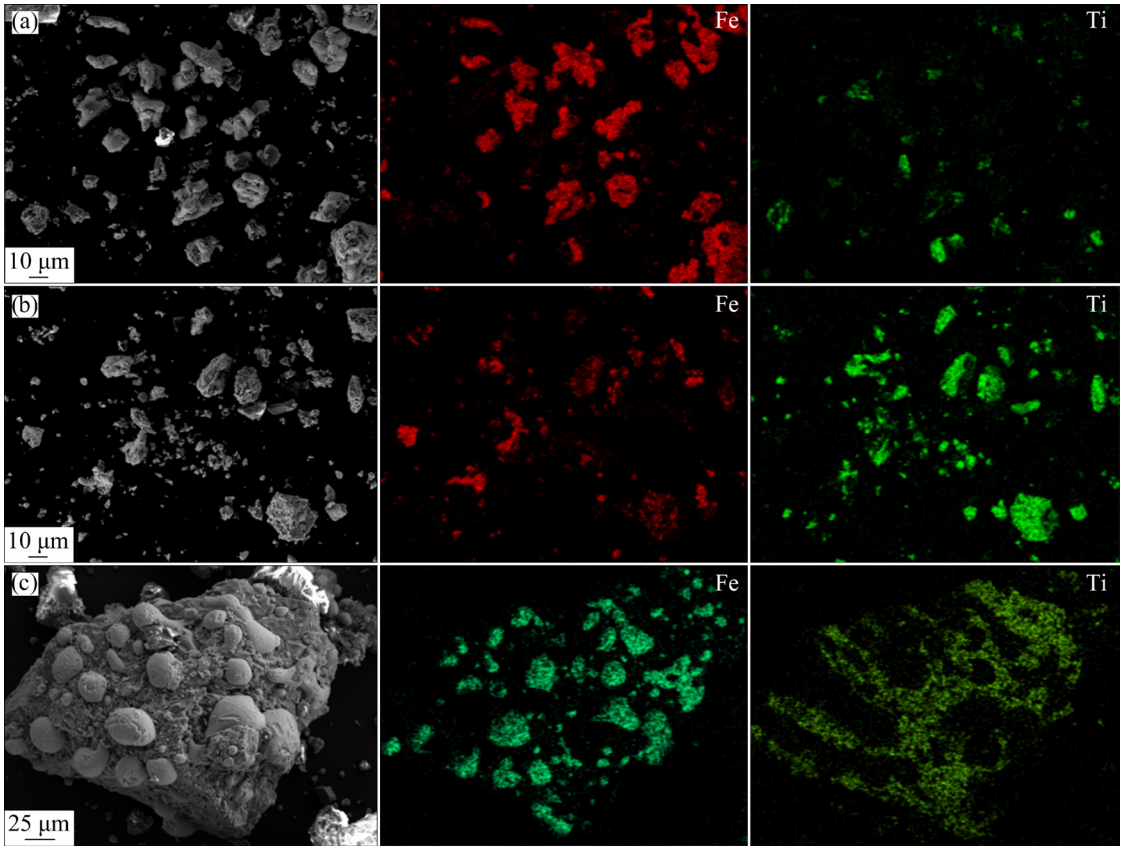

Fig. 6 SEM images and EDS mapping of (a) iron ore concentrate, (b) ilmenite concentrate and (c) raw ore reduction products (1140 °C, 3 h, C-to-Fe molar ratio of 1.2:1)

Consequently, enhancing the reduction procedure becomes imperative for optimizing the reduction process.

3.3 Effect of pre-oxidation on reduction of raw ore

3.3.1 Phase composition transformation in pre-oxidation process

The iron concentrate, titanium concentrate, and raw ore underwent pre-oxidation at a temperature of 800 °C for 1 h. After pre-oxidation of iron concentrate and titanium concentrate, the primary phases observed are Fe_2O_3, and Fe_2O_3 with TiO_2 (Fig. S3 in SI), as indicated by Reactions (26) and (27). However, no TiO_2 phase is observed during the pre-oxidation of the raw ore (Fig. 7). Upon pre-oxidation at 700 °C, both Fe_3O_4 and $FeTiO_3$ significantly diminish, accompanied by the pronounced emergence of Fe_2O_3 peaks. Nevertheless, as the pre-oxidation temperature increases to 800 °C, the appearance of Fe_2TiO_5 peaks is noted, possibly stemming from the reaction between TiO_2 and $FeTiO_3$ (Reaction (6)). Additionally, Fig. S4

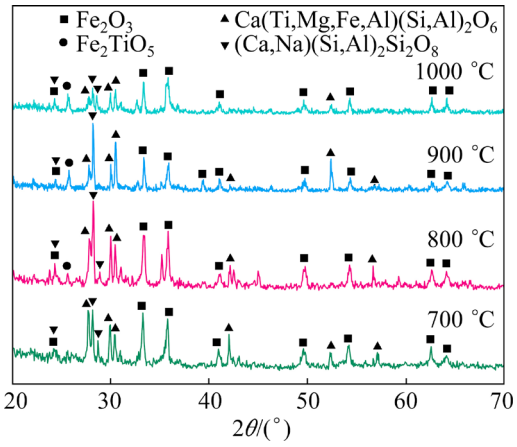

Fig. 7 XRD patterns of raw ore after pre-oxidation at different temperatures

(in SI) presents the XPS spectra of the raw ore and pre-oxidation samples, and the XPS data are summarized in Tables S1 in SI. It is demonstrated that the oxidation of iron is completed upon roasting at temperatures exceeding 800 °C. Upon further elevation of the oxidation temperature, there is no change in the phase composition, but distinct differences of the microstructural characteristics are

observed (Fig. 8).

$$2Fe_3O_4+1/2O_2=3Fe_2O_3 \quad (26)$$

$$2FeTiO_3+1/2O_2=Fe_2O_3+2TiO_2 \quad (27)$$

$$FeTiO_3+TiO_2=Fe_2TiO_5 \quad (28)$$

Figure 8 illustrates the metallographic microstructure of the raw ore before and after pre-oxidation at 900 °C. Bright minerals observed in the images correspond to magnetite, gray minerals to ilmenite, and dark minerals to silicate gangue. It is evident that the ilmenite in the raw ore exhibits a dense structure, whereas magnetite contains sporadic pores but generally presents a regular structure. After pre-oxidation, both mineral phases show an increase in porosity in their microstructures, accompanied by irregular edge morphologies.

3.3.2 Degree of metallization and reaction mechanism

Figure 9(a) shows the effect of pre-oxidation on the metallization degree of iron and ilmenite concentrate. By comparing the metallization degree of the pre-oxidized iron concentrate with that of the non-pre-oxidized iron concentrate, it is evident that the former exhibits a higher degree of metallization. Nevertheless, this difference in metallization degree is not deemed significant upon reaching a temperature of 1100 °C. The corresponding XRD analysis of the reduction products is presented in Fig. S5 in SI. It can be observed that the $FeTiO_3$ peak, indicative of pre-oxidized iron concentrate, is entirely absent. Instead, the formation of $(Mg,Fe)Ti_2O_5$ occurs at a temperature of 1050 °C, suggesting that pre-oxidation can enhance the reduction rate of iron and ilmenite concentrate.

Figure 9(b) illustrates the effect of pre-oxidation temperature on the metallization degree of the raw ore. As the roasting temperature escalates to 800 and 900 °C, the metallization degrees of the raw ore rise to 93.8% and 97.8%, respectively. However, at a roasting temperature of 1000 °C, the metallization degree experiences a decline to 90.7%.

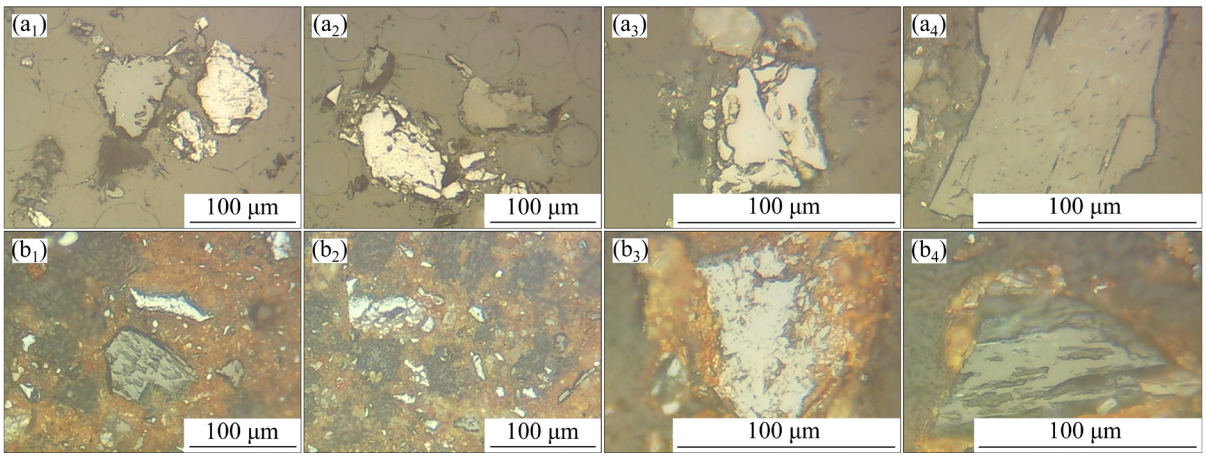

Fig. 8 Metallographic cross section images of raw ore (a_1−a_4) before and (b_1−b_4) after pre-oxidation at 900 °C

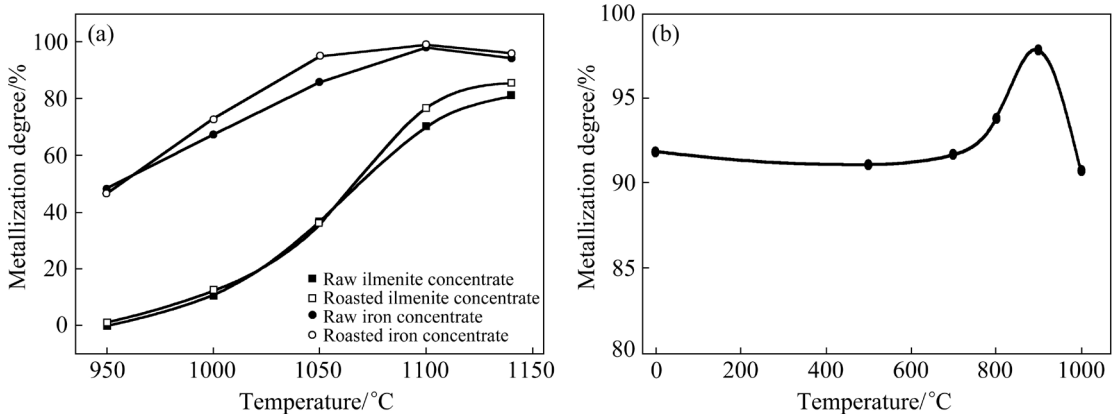

Fig. 9 (a) Effect of pre-oxidation on metallization degree of iron and ilmenite concentrate; (b) Effect of pre-oxidation temperature on metallization degree of VTM raw ore

This decrease can be attributed to sintering phenomena within the raw ore, leading to the compaction of magnetite and ilmenite surfaces, which impedes the reduction process. Figure S6 in SI presents the SEM images of the reduced samples subjected to different-temperature pre-oxidation. Upon pre-oxidation at 800 and 900 °C, the metallic iron in the resulting reduced products exhibits a pronounced tendency for aggregation, leading to the formation of larger overall metallic iron particles that are not integrated into the gangue surface. This phenomenon suggests that pre-oxidation enhances the reduction efficiency of magnetite by facilitating the early formation and aggregation of metallic iron particles, which subsequently grow into larger particles characterized by distinct distribution boundaries between iron (Fe) and titanium (Ti) as well as silicon (Si). Finally, the XRD pattern of the reduced sample obtained from pre-oxidized raw ore under optimum conditions is demonstrated in Fig. 10, where the main phases are Fe, (Mg,Fe)-Ti_2O_5, (Ca,Na)$(Si,Al)_2Si_2O_8$ and Ca(Ti,Mg,Fe,Al)-$(Si,Al)_2O_6$. In conclusion, considering both the metallization degree and the presence of discrete metallic iron monomer particles, the optimum pre-oxidation temperature for the raw ore is determined to be 900 °C, corresponding to a metallization degree of 97.8%.

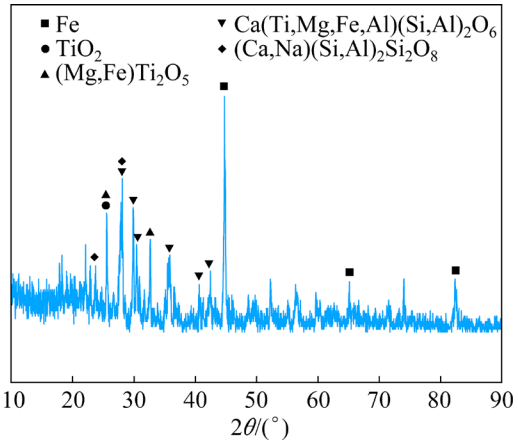

Fig. 10 XRD pattern of reduction product of pre-oxidized raw ore

3.4 Ball milling−magnetic separation process

To investigate the behavior of Fe and Ti during the magnetic separation process, grinding−magnetic separation was performed on the pre-reduced products under the afore-mentioned optimal conditions. Figure 11(a) illustrates the effect of the magnetic field intensity on the recovery of Fe and Ti in the resulting magnetic separation slag. As the magnetic field intensity varies in the range of 50−250 mT, the content of Fe and Ti within the magnetic separation slag exhibits a declining trend, decreasing from 3.66 wt.% and 8.99 wt.% to 2.68 wt.% and 8.81 wt.%, respectively. Consequently, the recovery of Fe and Ti also experiences a decrease, declining from 8.1% and 77.2% to 5.8% and 74.4%, respectively. These observations suggest that increasing the magnetic field intensity significantly facilitates the separation of magnetic metallic iron from the reduced products.

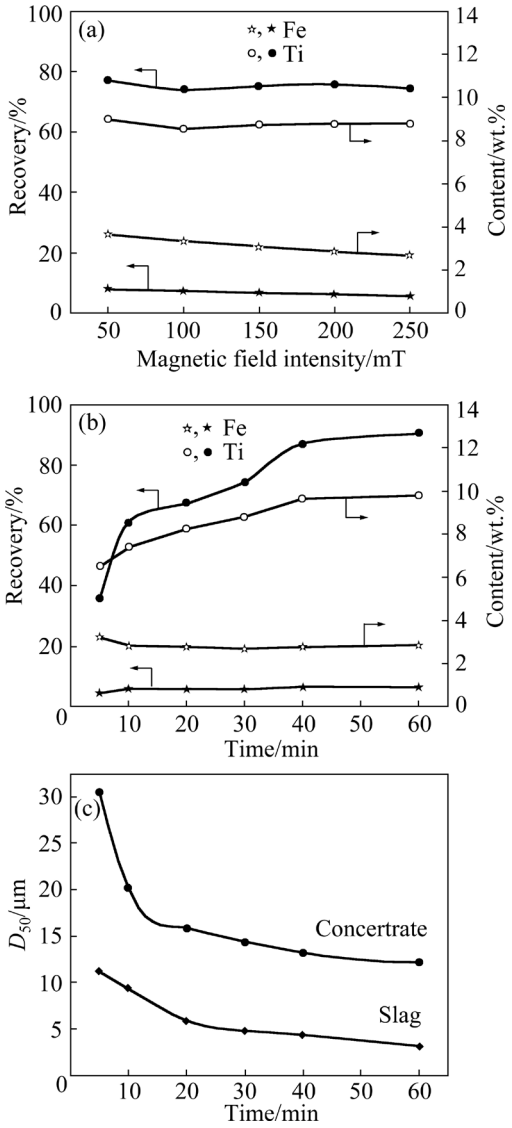

Fig. 11 Effect of (a) magnetic field intensity and (b) ball milling time on recovery and content of Fe and Ti in magnetic separation slag; (c) Effect of ball milling time on particle size

In Fig. 11(b), it can be observed that an increase in ball milling time from 5 to 40 min leads to a significant enhancement in both the content and recovery of Ti in the magnetic separation slag. Specifically, the Ti content and recovery escalate from 6.51% and 36.05% to 9.65% and 87.07%, respectively. Conversely, the effect of ball milling time on Fe content and recovery is relatively minor. In addition, Fig. 11(c) presents the influence of ball milling time on the particle size of the magnetic separation slag and concentrate. As the ball milling time increases, the particle sizes of both the magnetic separation slag and concentrate decline progressively. Ultimately, when the ball milling time reaches 40 min, the particle sizes of the magnetic separation slag and concentrate diminish to 4.33 and 13.23 μm, respectively.

In conclusion, the optimal reduction and magnetic separation conditions are as follows: pre-oxidation temperature of 900 °C, reduction temperature of 1140 °C, reduction time of 3 h, C-to-Fe molar ratio of 1.2∶1, ball milling time of 40 min, and magnetic field intensity during magnetic separation of 250 mT, and the composition of magnetic concentrate and magnetic separation slag obtained under these conditions are given in Table 3. The magnetic separation slag has a Ti grade and recovery of 9.36% and 87.07% respectively. The magnetic concentrate obtained from the magnetic separation has an Fe grade and recovery of 76.78% and 93.41%, respectively. Additionally, V in the slag has a grade and recovery of 0.15% and 85.53%, respectively. The trend of V is consistent with that of Ti, as most of it enters the magnetic separation slag.

Table 3 Chemical composition of magnetic phase and magnetic separation slag (wt.%)

Sample	TFe	V_2O_5	TiO_2	SiO_2	Al_2O_3	CaO	MgO
Magnetic phase	76.78	−	5.62	6.23	3.26	1.42	3.37
Magnetic separation slag	4.25	0.26	15.61	29.47	9.98	11.06	11.59

Figure S7 in SI illustrates the XRD pattern of the magnetic separation concentrate subjected to varying durations of ball milling. The XRD analysis reveals the presence of distinct constituents, including pyroxene, feldspar, and black ilmenite, within the magnetic separation concentrate when the ball milling is 5 min. This observation can be attributed to the fact that minerals exhibit larger particle sizes at shorter ball milling durations, leading to the entrapment of transient fossil phases within the metallic iron matrix. Consequently, these entrapped phases become incorporated into the magnetic separation concentrate without undergoing complete isolation. Furthermore, the $(Fe,Mg)Ti_2O_5$ phase, characterized by inherently weak magnetic properties, readily segregates into the magnetic fraction during the magnetic separation process. As the ball milling time is further prolonged, a noticeable reduction in the peaks associated with the $(Fe,Mg)Ti_2O_5$ phase becomes apparent. In fact, for ball milling duration surpassing 40 min, a substantial portion of these peaks dissipate, indicating a more comprehensive mineral separation process.

3.5 Mechanisms of metal iron particle formation and growth during direct reduction

As shown in Fig. 12, a comparative investigation was executed to elucidate the underlying mechanisms governing the formation and amplification of iron particles in the direct reduction process of both iron concentrate and raw ore. In the case of iron ore concentrate, the iron-bearing phase experienced reduction upon contact with the reducing agent, giving rise to the genesis of minute metallic iron particles. Subsequently, these particles underwent diffusion and coalescence, culminating in the formation of larger metallic iron particles during the subsequent stages of heating and reduction. In contrast, owing to the relatively modest iron content within the raw ore, a limited quantity of metallic iron particles were engendered, thereby diminishing the prospects for particle aggregation and growth. Furthermore, the presence of a substantial quantity of silicate gangue in the raw ore impeded the diffusion and coalescence of iron particles. This hindrance was exacerbated by the emergence of a partially molten liquid phase under elevated-temperature conditions, which led to the ensnarement of numerous metallic iron particles within the gangue, consequently hindering their growth. However, it was observed that pre-oxidation served to augment the reduction reactivity of the raw ore, facilitating the generation of an increased number of metallic iron particles

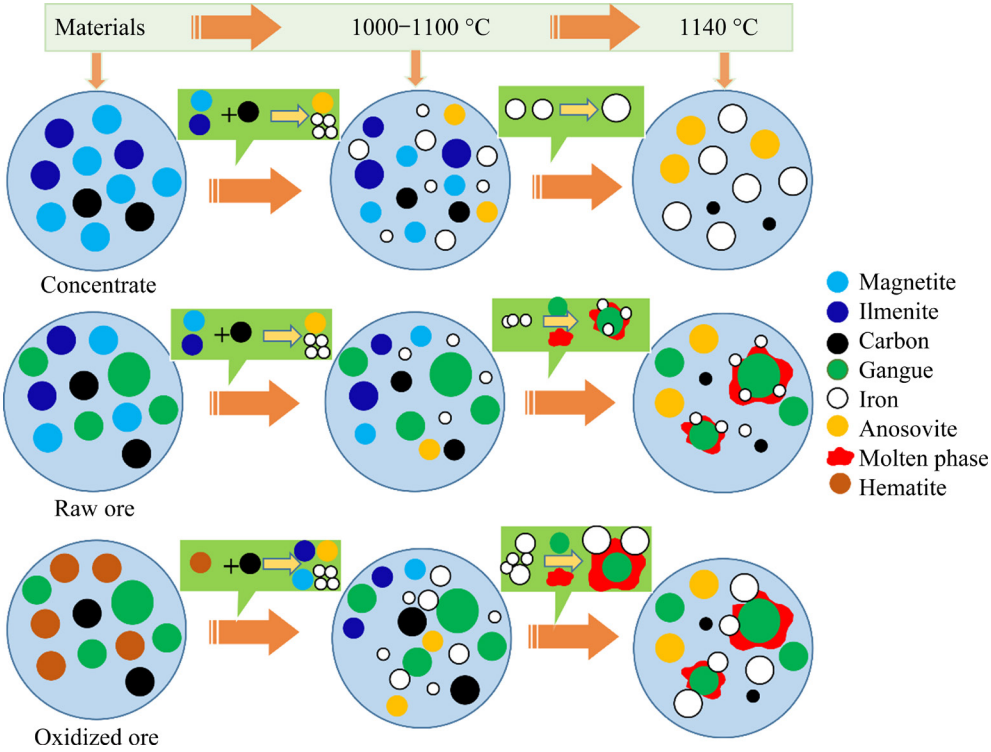

Fig. 12 Mechanism of formation and growth of metal iron particles during reduction

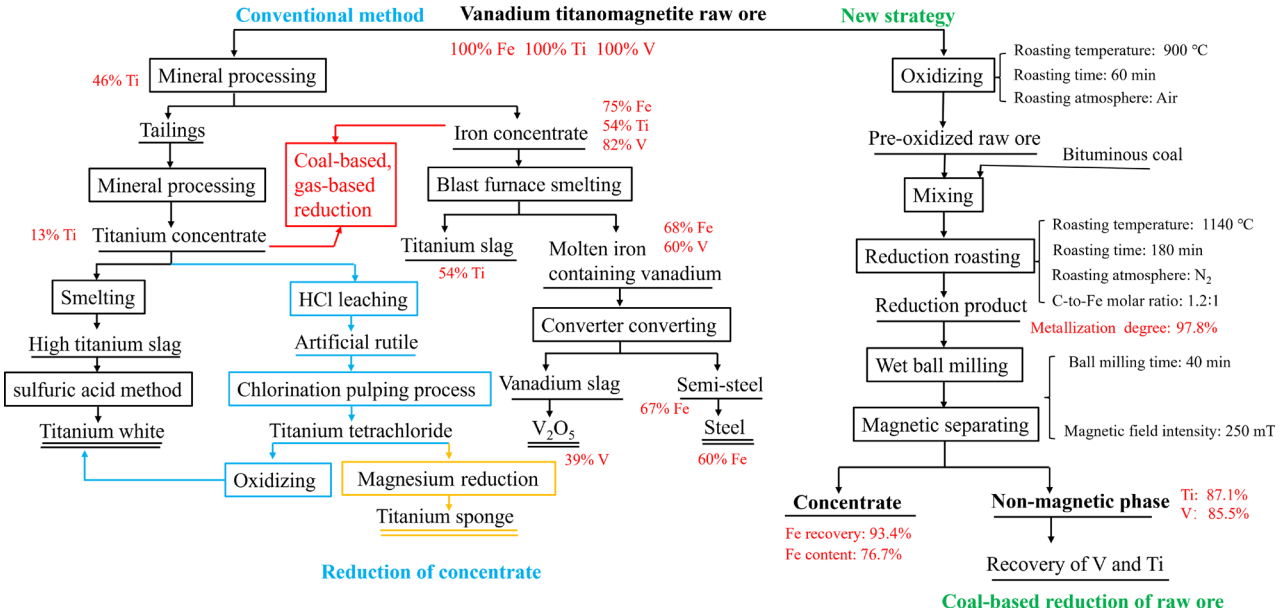

Fig. 13 Flow chart of coal-based direct reduction of VTM raw ore and conventional method

even at relatively low temperatures, thus elevating the probability of particle aggregation. Following the emergence of larger metallic iron particles, even if some of them became enclosed within the gangue due to the presence of the molten liquid phase, their expanded dimensions rendered them amenable to easier separation in subsequent grinding and magnetic separation procedures.

Compared to the traditional utilization process of VTM raw ore (Fig. 13), the loss ratio of titanium with new approach is reduced from 54% to 12.9%, thus mitigating the generation of currently unusable titanium-containing slag. Subsequent work will focus on further investigating cleaner hydrogen reduction, providing a suitable and sustainable solution for future production.

4 Conclusions

(1) At a reduction temperature of 1140 °C, reduction time of 3 h, and C-to-Fe molar ratio of 1.2∶1, the metallization degree of iron in the VTM raw ore is 91.8%. During the reduction process, primarily iron oxides undergo reduction, while gangue phases barely participate in the reaction. In addition, the growth and aggregation of metallic iron particles are hindered by the gangue.

(2) The direct reduction of raw ore process is enhanced by pre-oxidation, where the optimal metallization degree of the raw ore is 97.8% after a 1 h oxidation roasting at 900 °C. Simultaneously, the particle size of iron particles in the reduced product significantly increases, allowing their existence as monomeric particles.

(3) Ultimately, magnetic separation yields a magnetic concentrate with a Ti content of 9.36 wt.% and an iron concentrate with an Fe content of 76.78 wt.%, achieving titanium and iron recovery efficiencies of 87.07% and 93.41%, respectively.

(4) The novel strategy proposed in this study significantly reduces the generation of currently unusable titanium-containing slag.

CRediT authorship contribution statement

Zheng-hao WANG: Methodology, Investigation, Experiment, Visualization, Writing − Original draft; **Si-yu CHEN:** Investigation; **Liang CHEN:** Investigation; **Bing LIANG:** Writing − Review & editing, Supervision; **Dong-mei LUO:** Conceptualization, Methodology, Writing − Review & editing, Funding acquisition.

Declaration of competing interest

The authors declare that they have no known competing financial interests or personal relationships that could have appeared to influence the work reported in this paper.

Acknowledgments

This work was funded by the National Natural Science Foundation of China (Nos. U20A20145, 51774205), and the Open Project from Engineering Research Center of the Ministry of Education, Sichuan University, China.

Supporting Information

Supporting Information in this paper can be found at: http://tnmsc.csu.edu.cn/download/21-p3480-2024-0026-Supporting-Information.pdf.

References

[1] WANG Shuai, GUO Yu-feng, JIANG Tao, YANG Lu, CHEN Feng, ZHENG Fu-qiang, XIE Xiao-lin, TANG Min-jun. Reduction behaviors of iron, vanadium and titanium oxides in smelting of vanadium titanomagnetite metallized pellets [J]. JOM, 2017, 69(9): 1646−1653.

[2] ZHANG Yi-min, WANG Li-na, CHEN De-sheng, WANG Wei-jing, LIU Ya-hui, ZHAO Hong-xin, QI Tao. A method for recovery of iron, titanium, and vanadium from vanadium-bearing titanomagnetite [J]. International Journal of Minerals, Metallurgy and Materials, 2018, 25(2): 131−144.

[3] ZHANG Yi-min, YI Ling-yun, WANG Li-na, CHEN De-sheng, WANG Wei-jing, LIU Ya-hui, ZHAO Hong-xin, QI Tao. A novel process for the recovery of iron, titanium, and vanadium from vanadium-bearing titanomagnetite: Sodium modification-direct reduction coupled process [J]. International Journal of Minerals, Metallurgy, and Materials, 2017, 24(5): 504−511.

[4] ZHANG Shu-shi, WANG Zhen-yang, HU Peng, RAO Jia-ting, ZONG Yan-bing, PANG Jing. Influence of composition and temperature on distribution behavior of V, Ti and Si in HIsmelt [J]. Transactions of Nonferrous Metals Society of China, 2023, 33(12): 3835−3846.

[5] HAN Ji-qing, ZHANG Jing, ZHANG Jia-hao, CHEN Xiao, ZHANG Li, TU Gan-feng. Recovery of Fe, V, and Ti in modified Ti-bearing blast furnace slag [J]. Transactions of Nonferrous Metals Society of China, 2022, 32(1): 333−344.

[6] FU Wei-guo, WEN Yong, CAI Xie. Development of intensified technologies of vanadium-bearing titanomagnetite smelting [J]. Journal of Iron and Steel Research, International, 2011, 4(18): 7−18.

[7] ZHOU Lan-hua, WANG Jun, GOU Shu-yun, CHEN Lv-ying, LI Ze-rong. Development of utilization of vanadic titanomagnetite [J]. Applied Mechanics and Materials, 2012, 184/185: 949−953.

[8] SUI Yu-lei, GUO Yu-feng, TRAVYANOV A, JIANG Tao, CHEN Feng, QIU Guan-zhou. Reduction roasting–magnetic separation of vanadium tailings in presence of sodium sulfate and its mechanisms [J]. Rare Metals, 2016, 35(12): 954−960.

[9] LIU Fu-hai, SUN Dong-bai, ZHU Rong, DONG Kai, BAI Rui-guo. Effect of side-blowing arrangement on flow field and vanadium extraction rate in converter steelmaking process [J]. ISIJ International, 2018, 58(5): 852−859.

[10] ZHAO Jin-xuan, WU Wei, ZHAO Bo, LI Xiang-chen, XIAO Feng. Influence of vanadium extraction converter process optimization on vanadium extraction effect [J]. Metals, 2022, 12(12): 2061.

[11] LIU Xue-jie, CHEN De-sheng, CHU Jing-long, WANG Wei-jing, LI Yong-li, QI Tao. Recovery of titanium and vanadium from titanium–vanadium slag obtained by direct reduction of titanomagnetite concentrates [J]. Rare Metals, 2022, 41(5): 1688−1696.

[12] LI Hui, HAN Yue-xin, JIN Jian-ping, GAO Peng, ZHOU Zhen-ya. Process mineralogy approach to optimize curing-leaching in vanadium-bearing stone coal processing plants [J]. International Journal of Mining Science and Technology, 2023, 33(1): 123−131.

[13] WANG Zheng-hao, CHEN Liang, QIN Zhi-feng, YANG Ke, LIANG Bin, ZHANG Guo-quan, LIU Chang-jun, LUO

Dong-mei. A green and efficient route for simultaneous recovery of low valence of vanadium and chromium, titanium and iron from vanadium slag [J]. Resources, Conservation and Recycling, 2022, 178: 106046.
[14] YANG Bi-wen, HU Yi-hang, LIU San-ping, ZHANG Xue-dong, ZHENG Chao-zhen, WANG Hai-bei. Influence of desulfurization slag containing oxides of vanadium and titanium on semi-steel pre-desulfurization [J]. Journal of Iron and Steel Research International, 2022, 29(6): 939−950.
[15] TAYLOR P R, SHUEY S A, VIDAL E E, GOMEZ J C. Extractive metallurgy of vanadium-containing titaniferous magnetite ores: A review [J]. Mining, Metallurgy & Exploration, 2006, 23(2): 80−86.
[16] YI Yi-hui, SUN Hu, YOU Jin-xiang, ZHANG Jin, CAI Yuan, ZHANG Xin, LUO Jun, QIU Guan-zhou. Vanadium recovery from Na_2SO_4-added V−Ti magnetite concentrate via grate-kiln process [J]. Transactions of Nonferrous Metals Society of China, 2022, 32(6): 2019−2032.
[17] FU Wei-guo, WEN Yong-cai, XIE Hong-en, DU M. Technologies and practices of BF intensified smelting of vanadium-bearing titanomagnetite at pangang [J]. Iron steel vanadium titanium, 2013, 34(3): 50−53. (in Chinese)
[18] LIU Wei-zao, TENG Liu-mei, ROHANI S, QIN Zhi-feng, ZHAO Bin, XU Chun-bao Charles, REN Shan, LIU Qing-cai, LIANG Bin. CO_2 mineral carbonation using industrial solid wastes: A review of recent developments [J]. Chemical Engineering Journal, 2021, 416: 129093.
[19] ZHAO Yong-qiang, ZHOU Wen-tao, LYU Xian-jun, SUN Ti-chang, AHMADZAI A. Effect of reducing agents on reducing atmosphere in coal-based direct reduction of beach titanomagnetite [J]. Journal of Central South University, 2022, 29(11): 3670−3677.
[20] SHI Yue, ZHU De-qing, PAN Jian, GUO Zheng-qi, LU Sheng-hu, XUE Yu-xiao. Investigation into the coal-based direct reduction behaviors of various vanadium titanomagnetite pellets [J]. Journal of Materials Research and Technology, 2022, 19: 243−262.
[21] LUO Yi, CHE Xiao-kui, CUI Xing-lan, ZHENG Qi, WANG Lei. Selective leaching of vanadium from V−Ti magnetite concentrates by pellet calcification roasting-H_2SO_4 leaching process [J]. International Journal of Mining Science and Technology, 2021, 31(3): 507−513.
[22] LI Feng, ZHAO Qing-jie, CHU Man-sheng, TANG Jue, LIU Zheng-gen, WANG Jia-xin, LI Sheng-kang. Preparing high-purity iron by direct reduction–smelting separation of ultra-high-grade iron concentrate [J]. International Journal of Minerals, Metallurgy and Materials, 2020, 27(4): 454−462.
[23] CHOI M E, SOHN H Y. Development of green suspension ironmaking technology based on hydrogen reduction of iron oxide concentrate: Rate measurements [J]. Ironmaking & Steelmaking, 2010, 37(2): 81−88.
[24] WANG Ming-yu, ZHOU Sheng-fan, WANG Xue-wen, CHEN Bian-fang, YANG Hao-xiang, WANG Sai-kui, LUO Peng-fei. Recovery of iron from chromium vanadium-bearing titanomagnetite concentrate by direct reduction [J]. JOM, 2016, 68(10): 2698−2703.
[25] CHEN Fu-rong, LV Wei, ZHOU Gang-wei, LIU Zhuo-liang, CHU Man-sheng, LV Xue-wei. Effects of pre-oxidation on the hydrogen-rich reduction of Panzhihua ilmenite concentrate powder: Reduction kinetics and mechanism [J]. International Journal of Hydrogen Energy, 2023, 48(36): 13415−13429.
[26] LUO Hong-lin, LIU Wei, QIN Wen-qing, ZHENG Yong-xing, YANG Kang. Cleaning of high antimony smelting slag from an oxygen-enriched bottom-blown by direct reduction [J]. Rare Metals, 2019, 38(8): 800−804.
[27] YAN Zheng-pei, ZHANG Ying, ZHENG Shi-li, ZHANG Yang, SUN Pei, SONG Zi-wei, SAFDAR Fai-za, QI Tao. Preparation of titanium mineral from vanadium titanomagnetite concentrates by hydrogen reduction and acid leaching [J]. Transactions of Nonferrous Metals Society of China, 2022, 32(9): 3099−3109.
[28] LIU Shui-shi, GUO Yu-feng, QIU Guan-zhou, JIANG Tao, CHEN Feng. Solid-state reduction kinetics and mechanism of pre-oxidized vanadium–titanium magnetite concentrate [J]. Transactions of Nonferrous Metals Society of China, 2014, 24(10): 3372−3377.
[29] GAO Yang, GUI Yong-liang, SONG Chun-yang, HU Bin-sheng, DU M. Present situation and prospect of comprehensive utilization of high titanium blast furnace slag [J]. Multipurpose Utilization of Mineral Resources, 2019, 40(1): 6−10.
[30] LV Wei, LV Xue-wei, XIANG Jun-yi, HU Kai, ZHAO Shi-qing, DANG Jie, HAN Ke-xi, SONG Bing. Effect of preoxidation on the reduction of ilmenite concentrate powder by hydrogen [J]. International Journal of Hydrogen Energy, 2019, 44(8): 4031−4040.

通过煤基直接还原钒钛磁铁矿提高铁和钛的回收率

王正豪，陈司宇，陈 良，梁 斌，罗冬梅

四川大学 化学工程学院，成都 610065

摘 要：提出煤基直接还原钒钛磁铁矿(VTM)原矿的新方法。结果表明，在较佳的还原条件(还原温度为1140 ℃，还原时间为3 h，碳/铁摩尔比为1.2:1，预氧化温度为900 ℃)下，铁还原金属化率为97.8%。最终，通过磁选获得的铁精矿的铁含量和回收率分别为76.78% (质量分数) 和93.41%，而磁选渣的钛品位和回收率分别为9.36% (质量分数) 和87.07%，钛损失率仅为12.93%。新方法能避免VTM原矿的选矿过程，有效减少铁精矿中钛的含量，提高有价金属的综合利用率。

关键词：钒钛磁铁矿；原矿；还原；预氧化；金属铁

(Edited by Bing YANG)